Research Article Vol. 33, No. 21 / 20 Oct 2025 / Optics Express 45446
Optics EXPRESS

High-energy X-ray radiography with apodized petawatt laser beams

TANNER NUTTING,[1,*] RICHARD ANTHONY,[1] FRANKO BAYER,[1] MILOŠ BURGER,[1] PAUL T. CAMPBELL,[1] FRANKLIN DOLLAR,[2] NICHOLAS P. ERNST,[1] REBECCA FITZGARRALD,[1] VICTOR FLORES,[2] CHRISTOPHER GARDNER,[2] BIXUE HOU,[1] IGOR JOVANOVIC,[1] GALINA KALINCHENKO,[1] GALINA KURANZ,[1] JOSHUA LEWIS,[2] WILLIAM LIKES,[1] YONG MA,[1] MONICA MASHKEVICH,[1] JOHN NEES,[1] GREGG SUCHA,[1] ALEXANDER G. R. THOMAS,[1] JOSEPH TO,[2] RICHARD VAN CAMP,[1] MICHAEL WENDT,[1] LOUISE WILLINGALE,[1] GRANT YOUNG,[1] QING ZHANG,[1] KARL KRUSHELNICK,[1] AND ANATOLY MAKSIMCHUK[1]

[1]*Gérard Mourou Center for Ultrafast Optical Science, University of Michigan, 2200 Bonisteel Boulevard, Ann Arbor, Michigan 48109, USA*
[2]*STROBE, NSF Science and Technology Center, University of California, Irvine, California 92617, USA*
[*]*tnutting@umich.edu*

Abstract: We have produced laser wakefield-accelerated electron beams with energies of 2 GeV in Target Area 1 of the ZEUS facility. These electron beams oscillate in the accelerating structure that is produced in the wake of an ultrashort laser pulse (25 fs). These 'betatron' oscillations result in the emission of a collimated (4 mrad divergence) beam of high-energy X-ray/gamma photons (on the order of several hundred keV). In this work, we demonstrate the capabilities of the ZEUS laser system by showing that apodizing the laser beam in the near field allows for the production of high-quality betatron X-rays for radiography purposes. This demonstrates that a high-power, large-aperture laser beam could be split into multiple parts to drive betatron X-ray sources from multiple angles or temporal delays into a High Energy Density (HED) target to be probed, enabling pump-probe measurements at multiple temporal delays or tomography on a single shot.

1. Introduction

Laser wakefield accelerators (LWFA) [1] have become a leading technology for advanced particle acceleration enabled by the spread of high powered lasers [2]. LWFA requires these high power laser pulses to drive relativistic electron plasma waves. During this process, electrons can be trapped in the accelerating structure which is formed from the electron plasma waves produced in the wake of the driver laser pulse. This process occurs in underdense plasmas (10^{17}cm^{-3} – 10^{19}cm^{-3} for an 800 nm laser) and requires laser intensities above 10^{18} W/cm^2. The acceleration gradients produced with laser wakefield acceleration are favorable in comparison to conventional accelerators, enabling the production of high energy electron beams on the centimeter scale. The acceleration gradients in a conventional accelerator are limited to ~100 MV/m. Typical acceleration gradients in LWFA are on the order of 100 GV/m [3] and electron beams with energies greater than 10 GeV have been experimentally demonstrated [4,5]. Additionally, high charge [6], high repetition rate [7,8], and high quality electron beams [9–11] have been demonstrated using LWFA.

#575286
Journal © 2025
https://doi.org/10.1364/OE.575286
Received 1 Aug 2025; revised 26 Sep 2025; accepted 3 Oct 2025; published 17 Oct 2025

During the acceleration process, the electrons undergo transverse oscillations, emitting X-rays in the direction of electron beam propagation. These betatron X-rays make LWFAs attractive candidates for advanced photon sources [12,13]. One of the unique properties of the betatron X-rays are their small source sizes, on the order of several microns [14]. This allows for high resolution imaging of small objects [15,16]. In recent years, high energy betatron radiation was produced with 2 GeV electron beams, yielding critical energies of 515 keV [17]. The high energy betatron photons produced in this work were used for imaging dense objects, offering an alternative to other laser driven MeV photon sources [18,19].

The on-axis spectrum of the betatron radiation from wiggler regime LWFA sources can be approximated by a synchrotron spectrum given by,

$$\frac{d^2I}{d\omega d\Omega} \approx N_\beta \frac{3e^2\gamma^2}{2\pi^3\hbar c\epsilon_0}\left(\frac{\omega}{\omega_c}\right)^2 K^2_{2/3}(\omega/\omega_c) \tag{1}$$

where ω is the frequency of the photons and ω_c is the critical frequency which defines the spectrum [20]. I is the intensity of the radiation, Ω is the solid angle, N_β is the number of oscillations per electron, and $K_{2/3}$ is a modified Bessel function of the second kind. The critical energy of the synchrotron spectrum, $E_c = \hbar\omega_c$ can be written in practical units as,

$$E_c[\text{keV}] = 1.1 \times 10^{-23}\gamma^2 n_e[\text{cm}^{-3}] r_\beta[\mu\text{m}] \tag{2}$$

where γ is the Lorentz factor of the accelerated electrons in a plasma with electron density n_e. The amplitude of the betatron oscillations, r_β can be approximated by measuring the source size, $\sigma = 2r_\beta$. Changing the plasma density or acceleration parameters such as acceleration length can change the energy of the electron beams and therefore the properties of the betatron radiation.

Betatron X-rays offer a means of high brightness, high resolution, and high energy photons at high repetition rate. These sources are also ultrashort in duration and can vary in energy from several keV to MeV. These characteristics are useful for the imaging of High Energy Density (HED) systems relevant to fusion plasmas. This capability is especially relevant as laser-driven imaging tools evolve to meet the demands of inertial confinement fusion (ICF) and future inertial fusion energy (IFE) systems. The development and demonstration of such high-resolution, high-energy X-ray sources support ongoing efforts to bridge diagnostic gaps in high repetition rate, high brightness environments central to IFE research. Betatron X-rays have been used to study laser-driven shocks [21] and would be ideal for resolving features on the order of the Liepmann–Taylor scale [22], a key length scale for turbulent plasmas. Prior work at large-scale ICF facilities, such as the National Ignition Facility (NIF), has demonstrated the importance of advanced X-ray diagnostics for resolving hydrodynamic instabilities in HED plasmas [23]. These efforts highlight the critical need for high spatial resolution and contrast in radiographic systems for imaging phenomena such as Rayleigh–Taylor instabilities [24]. Similarly, X-ray imaging has been employed to investigate mixing and the transition to turbulence in laser-driven counterflowing shear flows [25], as well as to determine density profiles in shock-compressed matter [26]. Our work contributes to this growing body of diagnostic capabilities by demonstrating a flexible, compact, high-resolution X-ray source suitable for future IFE environments and relevant to emerging high repetition rate, petawatt-class laser systems. The advantage of using high energy betatron X-rays in the 100 keV range [17] to probe IFE plasmas is tied to the fact that standard ICF/IFE sources self-emit predominantly at much lower photon energies. The hohlraum drive is measured within the soft X-ray range (> 1 keV) [27]. The capsule's hot-spot self-emission is well described by a thermal bremsstrahlung continuum corresponding to electron temperatures of only a few keV and the spectrum is exponentially suppressed at tens to hundreds of keV [28]. In the ~100 keV range, the fusion target's intrinsic self-emission is minimal, and background can be managed by line-of-sight, shielding, and timing.

Many of the scientific grand challenges in high-field science require two beams to interact in both space and time. For instance, in the case of laser Compton scattering to enable exploration of QED regimes of intense light, one petawatt-power beam is required to drive the interaction while a separate beam is required to be focused to high intensities [29]. Accessing TeV energies through staged LWFA is another area in which multiple high-power drivers are required to achieve scientific goals [30,31]. One approach towards this is to field multiple amplifiers, and so important is this goal that upcoming ultrahigh-intensity facilities like ELI-NP and NSF OPAL are being designed with multiple amplifiers to meet these needs [32,33]. However, due to the large cost and space requirements for petawatt amplifiers, a simpler approach such as beam splitting would be welcome. Two fundamental approaches to beam splitting are commonly used for low-power lasers, division of amplitude in which a laser passes through a plate that reflects a portion of the beam; and division of wavefront in which a fully reflective mirror reflects only a portion of the beam (e.g., a D-shaped or split mirror). These approaches have not been able to scale to petawatt peak powers. In the former case, nonlinear propagation through the dielectric (B-integral/self-phase modulation), material dispersion, and wavefront distortions from the beamsplitting optic place an upper limit on accessible intensity and relegate this technique to large-area probe or heating beams. With the latter technique, the high coherence of the beam means that sharp cuts from the splitting mirror introduce hard-edge diffraction that degrades the far-field, while the already high fluences risk laser-induced damage upon propagation [34].

In this work, we show the feasibility of X-ray imaging and phase contrast imaging with X-rays at the Zettawatt Equivalent Ultrashort pulse laser System (ZEUS) facility using LWFA produced betatron radiation. We demonstrate it is possible to produce these X-ray sources with various near field laser beam profiles. For example, we use an annular laser beam profile as well as a half beam to produce electron beams and betatron radiation. With this source, we perform high resolution radiography and phase contrast imaging as well as radiography of dense objects at low magnification. This demonstration could lead to splitting petawatt (PW) laser beams in the near field, allowing for redirection or temporal delay between the separated portions. This in turn enables dynamic targets to be imaged from different angles or at different times within a single shot of a PW laser, reducing cost and simplifying the co-timing of multiple beams. Additionally, the redirected beams can be used to drive betatron sources with different properties, opening the possibility for dual-energy radiography.

2. Apodization and focal spot characterization

We show that apodized laser beams, produced by altering the near field profile of the laser, can be used to produce a betatron X-ray source. This is important because it enables applications such as single shot, multi-view angle, and multi-temporal delay imaging of HED targets. For example, a multi-view angle application is illustrated in Fig. 1(a). This geometry uses the 'half beam' apodization to split a single betatron driver laser pulse into two legs which can be redirected to view a target from two different angles on the same shot. In principle, the beam could be split into even more parts, limited only by the energy and aperture of the laser pulse, such that the normalized vector potential, $a_0 \geq 1$. This splitting of the beam could occur in vacuum, after compression. This is difficult to do with beam splitters post compression because of damage and nonlinearities within the bulk of the optic. Given a sufficiently energetic laser pulse and an appropriate splitting optic, it would be possible to produce a tomographic reconstruction of an HED (or industrial) plasma phenomenon with a single shot. It is important to emphasize that two or more deformable mirrors could be used to control focal spot shapes and focal positions of the beams after splitting, offering further flexibility.

As a proof of principle demonstration, we produced electron beams and betatron radiation with a single half of the beam. The apodizer used to produce this half beam is a sheet of white Teflon with a column of razor blades at the interface between the blocked and unblocked halves of the

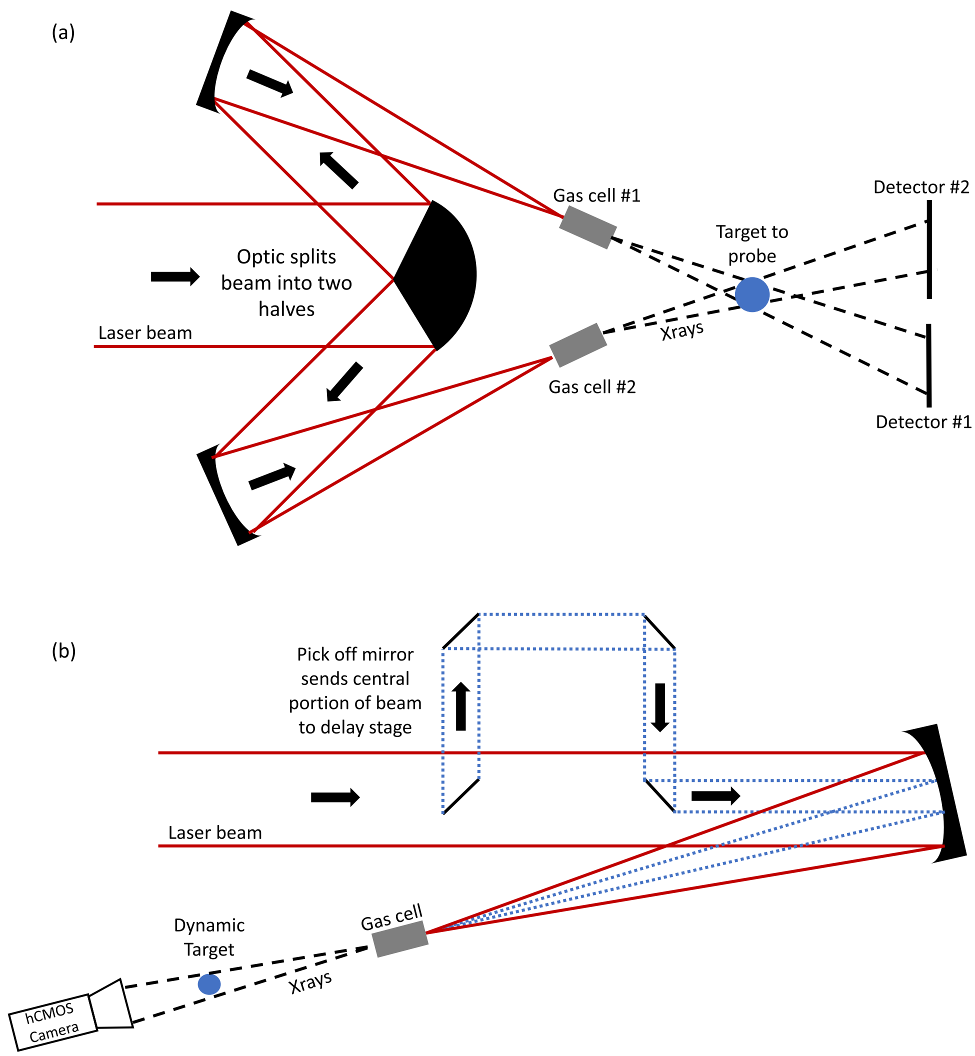

Fig. 1. Conceptual applications of apodized petawatt laser beams in the context of radiography. (a) Application of the half beam concept. An optic splits the laser pulse into two parts (although this is not a fundamental limit). The two parts of the laser beam are then sent to focusing optics which focus the split beams into two different gas cells that point into a target of interest at two different angles on the same shot. (b) Application of the annular beam concept. The central portion of the beam is picked off from the main beam. This central portion is delayed with respect to the main beam on the order of nanoseconds. The beams are then recombined on the same axis and are focused using the same focusing optic onto the same gas cell, producing betatron X-rays at two different temporal delays coming from the same angle. An hCMOS camera would be required to view the two images since this camera has as low as 2 ns inter-frame time.

beam. The razor blades are important for mitigating coherent diffraction effects at the interface between the blocked and unblocked portions of the beam. The maximum fluence on the gratings we observed with this technique was 90 mJ/cm^2. This fluence is typical of the unapodized beam as well.

Optics EXPRESS

The annular beam profile shown in this work would be useful for producing two betatron sources at the same angle into a target but delayed on the nanosecond time scale to see how the target evolves. An illustration of this concept is shown in Fig. 1(b). At the ZEUS laser facility at the University of Michigan, we have successfully separated the central 7.62 cm diameter section of the beam from the remaining annular portion of the beam by using a pick off mirror. We then delayed this central portion with respect to the annular portion and reintroduced the central part of the beam onto the same path as the annular beam prior to arrival at the focusing mirror. The primary advantage of this method is that only one focusing mirror needs to be used. Note also that the central part of the beam and the annular part of the beam will be focused with different f/#'s. This would lead to different electron beam properties and therefore different betatron X-ray properties. These could be characterized prior to a probing experiment and then could be used to diagnose different thicknesses of material on the same shot or regions of different plasma density, for example. The detector in this case could be an hCMOS camera which captures 2 ns frames with an inter-frame time on the order of nanoseconds [35,36].

During this proof of principle experiment, we also used the annular portion of the beam to produce electron beams and betatron radiation. The apodizer used in this case was a 7.62 cm diameter circular piece of Teflon that was concentric with the laser beam. Along the perimeter of this Teflon piece were razor blades which mitigated the diffraction along the edges of the apodizer. The post that held the circular apodizer was protected with a column of razor blades. The apodization in this experiment took place before the compressor because this allowed us to change the laser beam near field without needing to vent the compressor or target chambers.

An important part of this concept is the focusability of the laser pulse after apodization. In Fig. 2 we show the near field profile of the full laser beam, the annular beam, and the half beam. Below each near field profile are the corresponding focal spots. The focal spots shown are stable at the mJ level, the energy level at which we can measure the focus on the camera. The shot to shot fluctuation of the RMS wavefront error for beams that produce these spots ranges from 0.04 to 0.08 waves for each apodization case. The near field profiles were obtained by using large (35.56 cm) sheets of burn paper. The burn patterns were taken with the fully amplified beam and were scanned immediately after collection. The far field images were acquired with a Basler CCD with 3.45 µm pixels. To correct the wavefront of the laser beam during this experiment, a necessary step in producing these focal spots, we used a PHASICS wavefront sensor and a 31 cm diameter ISP System deformable mirror operating in closed loop mode. Two deformable mirrors were used in the setup, one before compression and one after apodization and compression. The use of two deformable mirrors provides additional flexibility in the experiment configuration. The closed loop was run and optimized with the full beam. Each of the focal spots shown in the figure used the same deformable mirror settings that were obtained by optimizing the full beam. Achieving high quality focal spots from petawatt class laser facilities is an ongoing challenge in the field. Making a focus with a near perfect Strehl ratio would necessitate a long campaign of optimization between grating alignment to remove spatial chirp, and the two deformable mirrors used to maintain the wavefronts necessary in both the compressor and the focusing plane. More commonly, foci such as those presented in Fig. 2 are used as an acceptable tradeoff of optimization and time. Note also that it is possible to apodize to circular near-fields which could enable more symmetric focal spots.

We have simulated the expected focal spot shape with a Fraunhofer diffraction calculation for an idealized version of each apodized near field profile. The simulated far field patterns corresponding to each of the near field profiles are shown in Fig. 2. When focusing the annular near field in simulation, the far-field pattern exhibits a distinct ring surrounding the central spot. This effect is related to the focal spot measurement of the annular beam in the lab, which shows increased energy in the wings of the pulse. In the case of the half beam, the simulated far field

Optics EXPRESS

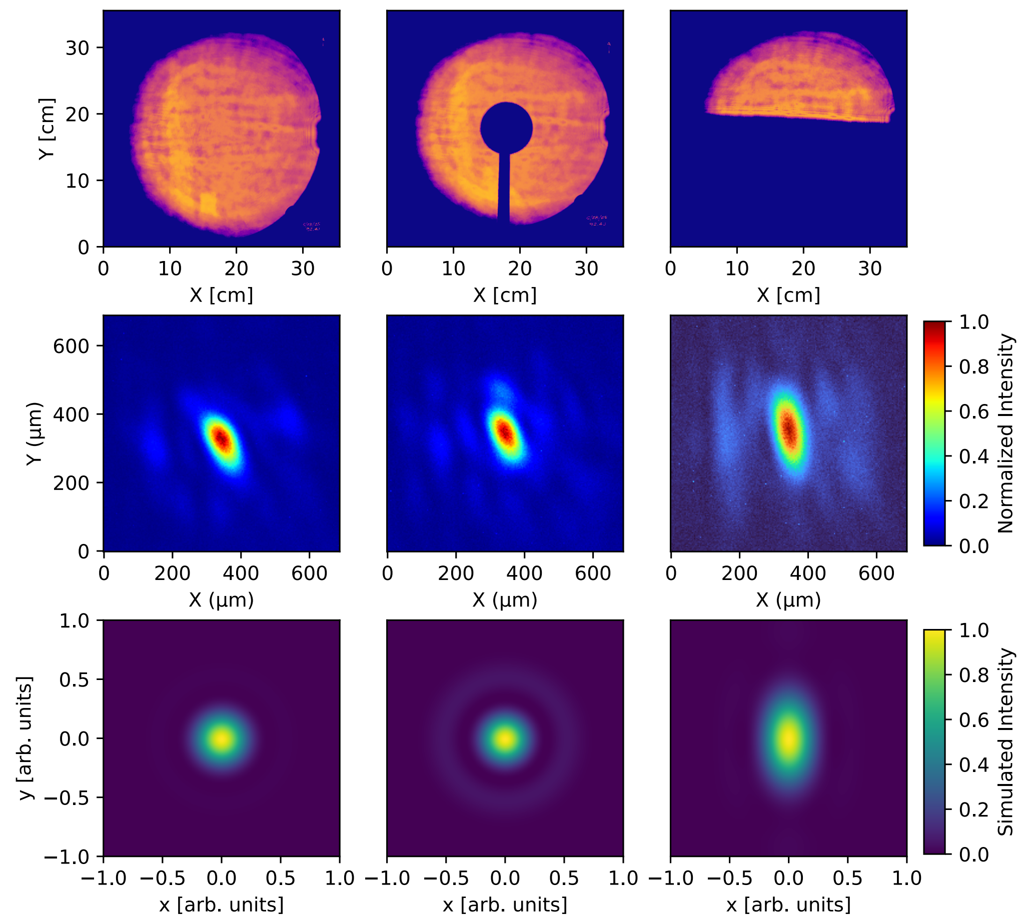

Fig. 2. Near field laser burn patterns, focal spot measurements, and far field simulations. (Top row) Near field burn profiles of the full beam and two different apodized near fields. The burn patterns were taken immediately before compression. (Middle row) Measured focal spots for the corresponding near field laser beam profile. Corresponding near fields are in the same column. (Bottom row) Simulated focal spots calculated using Fraunhofer diffraction. The corresponding near fields for these simulated spots are idealized versions of the near fields used in the experiment.

pattern is elliptical. This corresponds to the measurement of an elliptical focal spot taken in the lab.

3. Experimental setup

The ZEUS laser at the University of Michigan was used to perform this experiment. The laser was nominally operated with an average laser energy of 49.1 J ± 0.6 J pre-compression. The throughput to the target chamber was measured to be 57%, resulting in 28.0 J on target. The pulse duration was measured to be 25 fs, resulting in a laser power of 1.12 PW on target. The focusing optic was a spherical mirror with a focal length of 18.92 m. The diameter of the full beam was measured to be 31 cm, resulting in an f/# of 61. For the full beam, the full width at half maximum (FWHM) of the focal spot was measured to be 72 µm by 107 µm. The radius at which

Optics EXPRESS

50% of the focal spot energy is contained was calculated to be 97 µm. This results in an intensity of 3.8 $\times 10^{18}$ W/cm^2 and a corresponding normalized vector potential, a_0 of 1.3. The focal spot of the annular beam had a 50% energy encircled radius of 110 µm, resulting in an intensity of 2.7 $\times 10^{18}$ W/cm^2 and an a_0 of 1.1. The half beam focal spot had a 50% energy encircled radius of 117 µm, giving an intensity of 1.3 $\times 10^{18}$ W/cm^2 with an a_0 of 0.8. The ZEUS laser is a Ti:Sapphire laser with a wavelength spectrum centered around 800 nm. Note also that the laser polarization was parallel to the surface of the table (i.e. horizontal). As discussed above, three different laser beam near field profiles were used during this experiment. Assuming a uniform energy distribution, it can be estimated (geometrically) that the nominal energy in the annular pulse is 93.75% that of the full beam. An energy measurement from a calibrated charge coupled device (CCD) indicated that the energy in the half beam was 24 J prior to compression. For each near field profile, the laser was focused onto the front of a 6 cm length gas cell which was filled with 97% He and 3% N_2 to produce electron beams via LWFA using ionization injection [37].

Prior to compression and apodization of the laser pulse, the beam was split using a 95% - 5% beam splitter. The main pulse was routed through the larger of the two compressors in the ZEUS facility while the less energetic portion of the beam was sent through the smaller of the two compressors. The less energetic portion of the beam was routed into the target area where it was used as a probe. The diameter of the probe beam was 10 cm since the beam is split prior to a telescope that expands the beam to a diameter of 31 cm. Transverse probing was employed to reconstruct plasma density profiles using interferometric measurements.

Simplified schematics of the experiment are shown in Fig. 3. The apodization of the laser beam occurs immediately before the compressor. Two setups were used for this experiment to demonstrate both the high resolution and high energy characteristics of the produced betatron X-rays. The first setup is a high magnification imaging setup intended to demonstrate phase contrast imaging and high-resolution radiographs. The laser was focused onto the front of the gas cell, producing electron beams and betatron radiation. After the interaction, the laser beam was reflected into a beam dump using 25 µm Kapton tape on a motorized tape drive spool. The tape drive was located 43 cm from the front of the gas cell. In the high magnification setup, the targets that were imaged were located 68 cm from the front of the cell. The electron beam was then swept by two 1 T magnets into DRZ-High scintillating screens in order to diagnose the electron spectrum. DRZ-High is a Gd_2O_2S:Tb scintillator. The field region of the magnets spans 30 cm longitudinally and the gap between the magnets is 10 cm. The X-rays were then filtered by two layers of 14 µm Al foil to protect the X-ray CCD from any stray laser light. The chip of the X-ray CCD was located 5.53 m from the front of the gas cell. In this configuration, the source to object distance was O = 68 cm and the object to detector distance was D = 553 cm. This resulted in a geometric magnification of M = D/O = 8.13×. The X-ray CCD used during this experiment was a Princeton Instruments SOPHIA-XO, Model ID SOP-2048BR-132-XO. This X-ray CCD has a 12 µm pixel size. Considering the geometric magnification of the system and the detector pixel size, and assuming that at least two pixels are required to resolve a feature, the minimum resolvable feature size is 2.95 µm.

The X-ray CCD which was used during this experiment is only sensitive to X-rays < 30 keV. To demonstrate radiography with the high energy betatron X-rays produced during this interaction, we changed our detector to a DRZ-High scintillating screen. This is a Gd_2O_2S:Tb scintillator with a resolution of 225 µm [38]. The photon absorption in the active layer of the DRZ-High scintillating screen provides a metric of the spectral response of the detector. The active layer is 310 µm thick and the absorption within this layer was calculated to fall to 10% at 149 keV and to 1% at 353 keV. The distance from the DRZ-High scintillating screen to the imaging camera's chip was 40 cm. As can be seen in Fig. 3(b), the angle between the incoming X-ray beam and the line of the sight from the center of the DRZ-High screen to the camera is 25.84 degrees. This was done to keep the camera away from the beam axis, reducing the number of hard hits on the

Optics EXPRESS

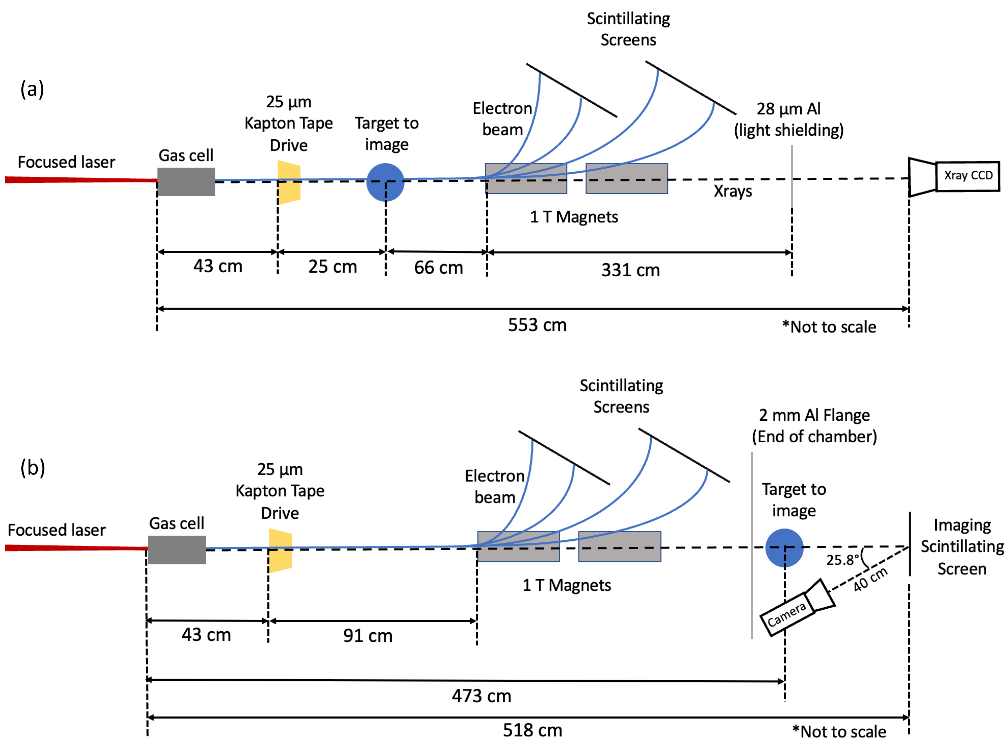

Fig. 3. Experimental setups. In both configurations the ZEUS laser beam from the PW beamline is focused onto the front of a 6 cm gas cell. High energy electrons undergo betatron oscillations and emit high energy X-rays. (a) Setup for high resolution X-ray imaging. The target is positioned 68 cm from the source in this configuration to provide a magnification of 8.13 ×. The detector in this case is an X-ray CCD that is only sensitive up to photons with energies up to 30 keV. (b) Setup for high energy X-ray imaging of dense objects. Target is positioned 473 cm from the source, providing a magnification of 1.1 ×. The detector in this case is a DRZ-High scintillating screen imaged with an objective lens.

CCD. This results in a spatial resolution that is horizontally nonuniform across the image due to a limited depth of field. This resulted in a minimum resolution of the imaging system of 158 µm on the beam axis. The minimum resolvable feature was plotted against the distance from the beam axis to reveal that the minimum resolution is constant for a range of 4 cm about the beam axis. The camera that was used to image the screen was a Basler a2A1920-51gmPRO with a 16 mm focal length objective lens. This radiography setup had a geometric magnification of 1.1×. The distance from the source to the object was O = 473 cm and the distance from the source to the detector was D = 518 cm. This is a notable result, as the target being imaged could be over 5 meters away from the source. This development enables new diagnostic approaches in experiments, addressing the issue of limited space near the target within the interaction chamber. Note also that the scintillating screen and the camera imaging it were located in air, immediately outside of the chamber. We machined a custom aluminum flange that is 2 mm thick in the center where the X-rays passed out of the end of the chamber.

4. Characterization of X-ray beam profiles and electron spectra

We used each near field laser beam profile to produce a betatron X-ray source. In Fig. 4, we show the betatron X-ray beam profiles taken on a DRZ-High screen. For each near field, we show the

X-ray beam profiles for two difference cases: i) A low divergence X-ray beam produced with a relatively lower plasma density and lower electron beam charge and ii) A higher divergence beam produced with a higher plasma density and higher charge electron beam. The results are summarized in Table 1. The table correlates the X-ray profile data to the electron spectra data for the selected representative shots. The high density case was used for the radiography applications. Factors that went into this decision included an increased betatron flux and the scale of the objects being imaged. Note that the color scale of the betatron profiles is in arbitrary counts. The laser beam that was used to obtain each profile is shown in the upper right corner of each profile. The relative counts between the annular and half beam profiles are appropriate to compare. However, the counts from the full beam are inflated due to a mid-experiment CCD triggering change done to avoid hard hits on the CCD. These hard hits can be seen in the full beam betatron profiles in Fig. 4(a). This characterization was necessary for the high energy radiography portion of the experiment, in which we aimed to demonstrate the high energy imaging capabilities on dense, macroscopic items found in the lab. The characteristics of the objects being radiographed called for a large beam with high flux. As will be discussed in the subsequent section, we prioritized source size and resolution for the second stage of the experiment.

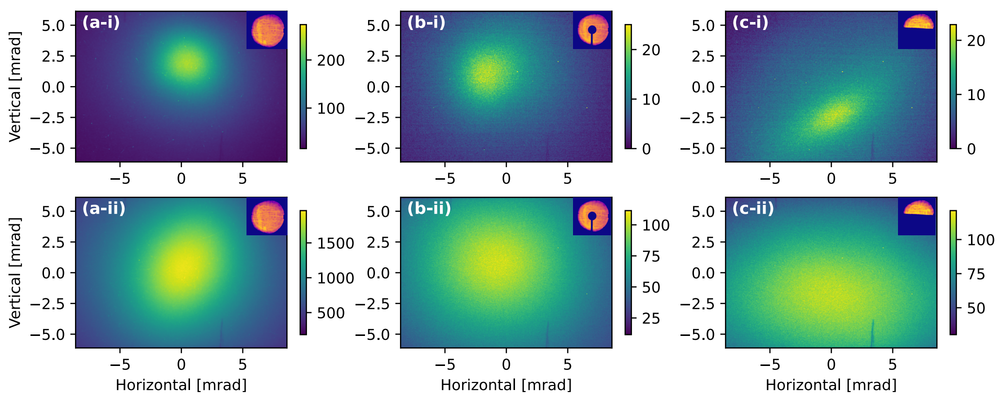

Fig. 4. Betatron profiles taken on DRZ-High screen. Perspective transforms were performed to account for the 25.8 degree angle at which the screen was imaged with the camera. Two cases are shown for each near field profile. The top row (a,b,c-i) shows betatron profiles from relatively low density plasmas, producing tightly collimated betatron profiles. The bottom row (a,b,c-ii) shows betatron profiles from higher density plasmas, producing more divergent betatron profiles with higher flux which were useful for imaging larger, dense objects.

Table 1. Plasma density, electron beam charge, and FWHM horizontal betatron divergence data for each X-ray profile/electron spectrum

Profile/spectrum	Laser near field	Plasma density	Electron beam charge	Betatron divergence
(a-i)	Full	$(4.8 \pm 0.5) \times 10^{17}$ cm^{-3}	44.9 ± 8.5 pC	6.7 ± 0.7 mrad
(a-ii)	Full	$(7.0 \pm 0.7) \times 10^{17}$ cm^{-3}	60.7 ± 11.5 pC	9.1 ± 1.0 mrad
(b-i)	Annular	$(9.7 \pm 1.0) \times 10^{17}$ cm^{-3}	11.8 ± 2.2 pC	7.4 ± 0.8 mrad
(b-ii)	Annular	$(1.3 \pm 0.1) \times 10^{18}$ cm^{-3}	31.3 ± 5.9 pC	12.8 ± 1.4 mrad
(c-i)	Half	$(1.1 \pm 0.1) \times 10^{18}$ cm^{-3}	8.6 ± 1.6 pC	16.0 ± 1.8 mrad
(c-ii)	Half	$(1.7 \pm 0.2) \times 10^{18}$ cm^{-3}	25.7 ± 4.9 pC	22.2 ± 2.4 mrad

The electron spectra corresponding to the plotted X-ray beam profiles are shown in Fig. 5. The figure is split into two regions along the energy axis corresponding the low and high energy scintillating screens, with plotted data spanning from 30 MeV to 470 MeV and 600 MeV to 2.2 GeV, respectively. Each near field profile was used to produce an electron beam for the two distinct cases of low (i) and high (ii) density plasma. Each spectrum has an inset showing the laser near field profile that was used. The spectra are independently normalized to their peak intensities. The charge for each of these beams is listed in Table 1.

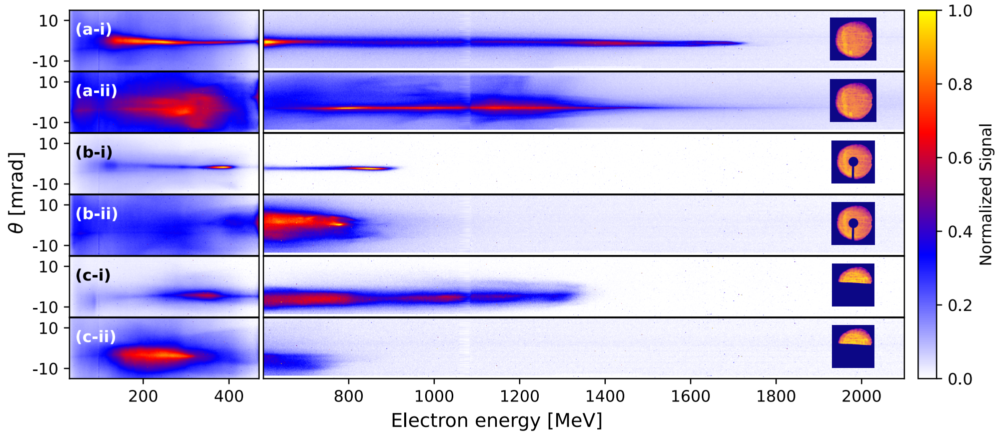

Fig. 5. Electron spectra used to produce the X-ray beam profiles shown in Fig. 4.

As demonstrated by the change in X-ray beam profiles and electron spectra, a critical parameter in the production of the betatron X-ray source is the plasma density [39]. The plasma density effects the electron beam properties and therefore the properties of the produced betatron X-rays. In Fig. 6(a), we show a trend that maximum electron energy decreases with increasing plasma density. Switching between near field profiles required corresponding adjustments in plasma density to maintain suitable betatron signal, likely due to reduced energy concentration in the central region of the focal spot. This reduction arises from both apodization (which decreases total energy) and imperfect wavefront correction (which increases energy in the wings). Using Eq. (2), the critical energy of the betatron spectrum is estimated to be 260 keV for the highest observed electron energy of 1.9 GeV. For the lower end of the observed electron energies (800 MeV), the estimated critical energy of the betatron spectrum is 80 keV.

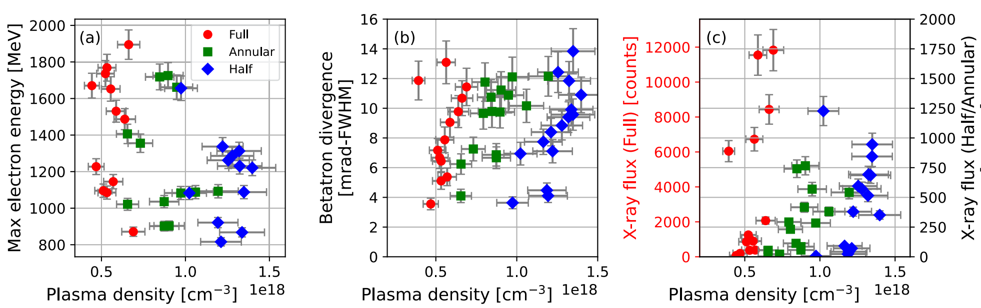

Fig. 6. (a) Maximum electron energy dependent on plasma density. Different near field profiles are shown in the legend. (b) Horizontal divergence of betatron X-ray beam as a function of plasma density. (c) X-ray flux for the full and annular/half beams as a function of density.

Optics EXPRESS

In Fig. 6(b), the FWHM divergence of the betatron beam in the horizontal direction is shown to increase with plasma density for each near field profile. At the lower density thresholds for each near field profile, collimated X-ray beams with divergences as low as ~4 mrad are observed. For higher plasma densities, the divergence ranges from 12 - 14 mrad. The clustering of data reflects the need to adjust plasma density for each profile to produce comparable X-ray signal for radiography under varying laser conditions.

In Fig. 6(c), we show that betatron X-ray flux increases with plasma density for each near field profile. The threshold densities for X-ray generation are inferred to be approximately 4.5×10^{17} cm^{-3}, 6.5×10^{17} cm^{-3}, and 9.5×10^{17} cm^{-3} for the full, annular, and half beams, respectively. Higher threshold densities for the apodized cases are a result consistent with the reduced energy in the laser focal region for such cases. Due to a change in CCD trigger timing, the flux values for the full beam should be interpreted separately from those of the apodized beams. The standard deviation of the pointing fluctuation of the betatron source was measured to be stable at 0.46 mrad, 0.57 mrad, and 0.52 mrad for the full, annular, and half beams, respectively.

5. High energy X-ray radiography of dense objects

A goal of this experiment was to demonstrate that the high energy betatron X-rays produced at the ZEUS laser facility could be used for radiography applications. Two high density objects that

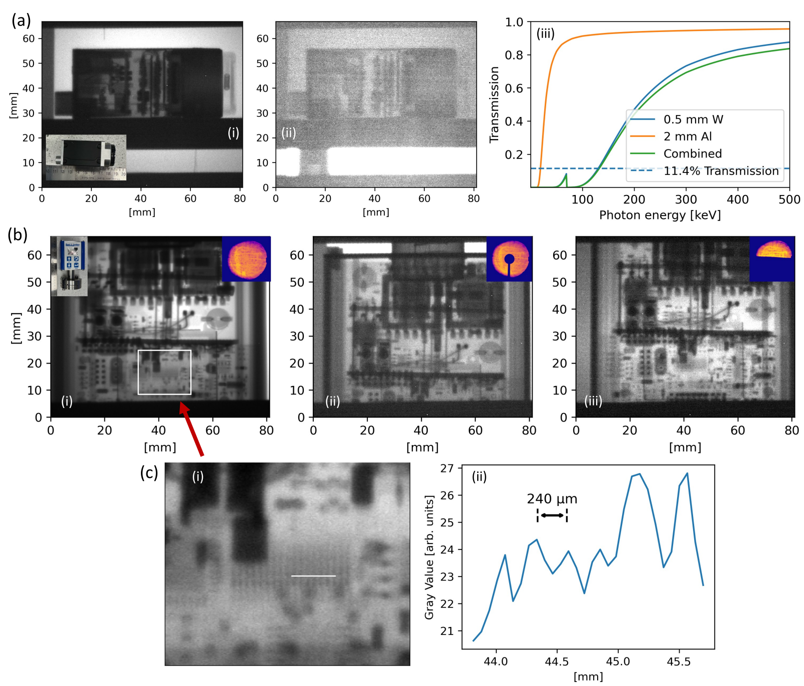

Fig. 7. **(a)** Radiographs of a Basler camera. These radiographs were taken with the full beam. (a-i) Basler camera through 2 mm of Al. (a-ii) Radiograph of the same camera with an additional 0.5 mm of W as a filter. (a-iii) The photon transmission curves of the two filter materials and the combined attenuation. **(b)** Radiographs of an ionization vacuum gauge taken with each laser near field profile. **(c)** Zoomed radiograph and a lineout of circuit features of the ionization gauge showing features as small as 240 µm being resolved. The lineout region is shown as a white line in the radiograph. This radiograph was taken with the full beam. A perspective transform was employed to account for the 25.8 degree viewing angle of the scintillating screen for all radiographs. Distances are in the object plane.

were radiographed are presented here. The first of which is a Basler camera shown in Fig. 7(a). These radiographs were taken with the full near field profile of the laser beam. Figure 7 (a-i) is a radiograph of the Basler camera through a 2 mm thick Al flange. The internal structure of the camera can be seen including the circuitry. Figure 7 (a-ii) shows a radiograph of the same camera, but through an additional 0.5 mm of tungsten (W). This 0.5 mm of tungsten highly attenuates any photons below 100 keV. This radiograph demonstrates the high energy of this betatron source. The transmission through 0.5 mm of W plotted against incident photon energy is included in the figure in panel (a-iii) [40]. To estimate the average photon energy on this shot, the relative transmission through the W sheet was calculated to be 11.4 %. By referring to the curve, it can be estimated that the average photon energy was 130 ± 8 keV for that shot. We deliberately allowed a hole to form in the Kapton tape drive by not moving it for 10 shots. After making a hole in the tape we observed radiographs of similar detail and signal, demonstrating that the 25 μm Kapton tape is producing a negligible amount of Bremsstrahlung radiation. This backs our claim that the source is from betatron radiation.

The second dense object radiographed and shown in this manuscript is an ionization vacuum gauge. In Fig. 7(b), the internal wiring of the ionization gauge can be seen. The X-rays producing these images travel through 2 mm of Al before reaching the target to be imaged. The ability to see through this metal vacuum gauge again demonstrates the high energy of the photon spectrum. A radiograph of the ionization gauge is shown for each laser near field profile. There are small features in the radiograph taken with the full beam that can be resolved down to 240 μm. A lineout of these features is shown in Fig. 7 (c-ii). The region of the lineout is shown as a white line on the zoomed in portion of the radiograph. The fact that this is the smallest resolvable feature could be a result of a convolution between the limiting resolution of the scintillating screen and the resolution of the imaging system. The imaging resolution at this position on the screen is 159 μm. Note also that the resolution being 240 μm does not necessarily mean that the source size is that large. Since the small features are slightly off axis, there could be some blurring due to the fact that the betatron emission is a line source [41,42].

6. High resolution and phase contrast imaging

The ability to resolve μm scale features is of importance for applications in HED plasmas as well as medical applications (i.e. imaging microcalcifications). As a part of this work, we used an X-ray CCD to image μm scale features with a magnification of 8.13×. We determined the best resolution for each of the laser beam near field profiles. In Fig. 8 we show radiographs of an XR Nanotech resolution target for each laser beam near field. Numbers near line features indicate the thickness of the lines in microns. Radiographs were taken using an X-ray CCD that is only able to detect photons with a maximum energy of 30 keV. Note that the smallest resolvable feature in the radiographs is approximately the source size. During the radiography experiment, the full beam and the annular beam were able to resolve 6±1 μm features and the half beam was able to resolve 5±1 μm features. The plasma densities for these measurements were 8.7×10^{17} cm^{-3}, 1.0×10^{18} cm^{-3}, and 1.4×10^{18} cm^{-3} for the full, annular, and half beam cases, respectively. Given the limited number of radiographs taken of the resolution target during the experimental campaign, it would not be appropriate to state that a given laser beam near field profile routinely produces betatron beams with a better resolution than the next. However, this does illustrate that each of these beam profiles are capable of producing X-ray sources with applications towards high resolution imaging.

To understand the density dependence of the betatron X-ray source size, the full beam was used in a 5 cm gas cell during a separate experimental campaign. The results of this density scan are shown in Fig. 9. The detector used for this study was the X-ray CCD. The source size was measured with the XR Nanotech resolution target. A minimum source size of 5 μm was

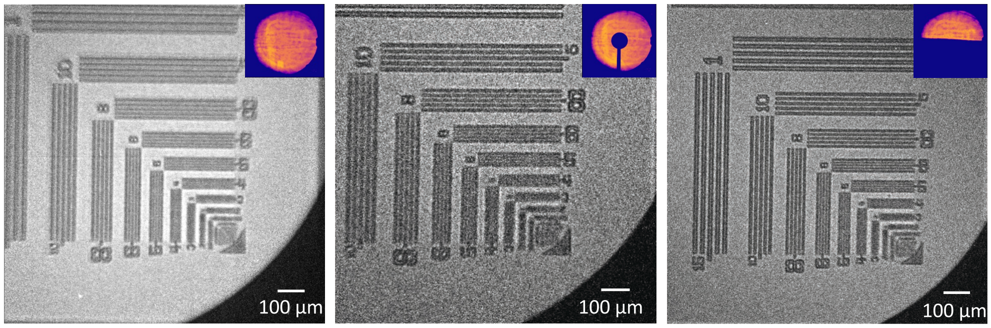

Fig. 8. Radiographs of a resolution target captured with an Xray CCD. The minimum resolvable features are 5 µm, implying the source size is approximately 5 µm. Radiographs of the resolution targets are shown for each laser beam near field profile.

obtained with plasma densities ranging from 5×10^{17} cm^{-3} to 8×10^{17} cm^{-3}. There is a trend of increasing source size with increasing plasma density.

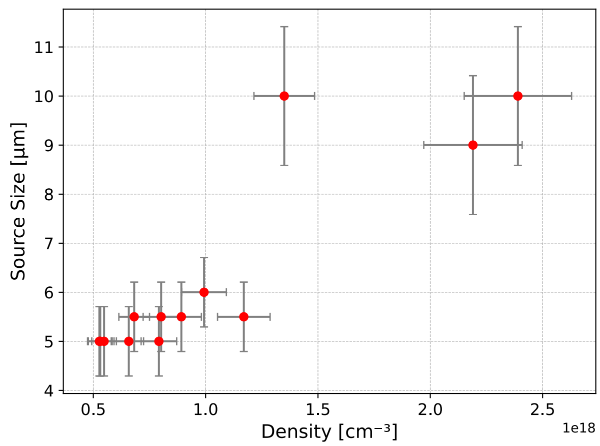

Fig. 9. Betatron X-ray source size vs. plasma density using the full beam in a 5 cm plasma. Plasma density was measured with interferometric techniques.

Given the small, µm scale source sizes of these X-ray beams, they are ideal candidates for phase contrast imaging. Phase contrast imaging is based on X-ray phase variations and is capable of producing high resolution images of low density and low atomic number objects or specimens in which there is little X-ray absorption [43]. To demonstrate phase contrast imaging, we imaged silica capillary tubes with two different inner diameters. In Fig. 10(a), the capillary on the left has an inner diameter of 74.4 µm and an outer diameter of 359.3 µm. The capillary on the right has an inner diameter of 149.6 µm and an outer diameter of 357.6 µm. A vertically summed lineout of the 149.6 µm inner diameter capillary is shown in Fig. 10(b). As can be seen in the lineout, there is clear edge enhancement at the inner walls of the capillary tube. This is evidence of phase contrast imaging produced by our spatially coherent source [44]. One of the regions of edge enhancement is circled in red. The laser near field profile used to produce the radiograph of the capillaries was the full beam. In Fig. 10(d), we show a radiograph of a capacitive target for HED experiments. Note also, that there is edge enhancement in the stalk that holds this target. This radiograph was taken with the annular laser beam profile. In Fig. 10(c), we show a radiograph of 1 mm diameter sodium polyacrylate spheres taken with the half beam. Internal defects can be

Optics EXPRESS

observed. These sodium polyacrylate spheres are of similar size to a National Ignition Facility (NIF) capsule, demonstrating the scale at which defects can be observed. Notice that the central portion of the right most sphere has a higher resolution than the other spheres or the outside of the same sphere. This is likely due to the fact that the X-ray source is a line source and the beam axis was slightly misaligned and in the upper right quadrant of the X-ray CCD chip. The transverse source size is small and on the order of a few microns. Slight deviations off axis lead to an effectively larger source size, blurring the radiograph in those regions [41,42].

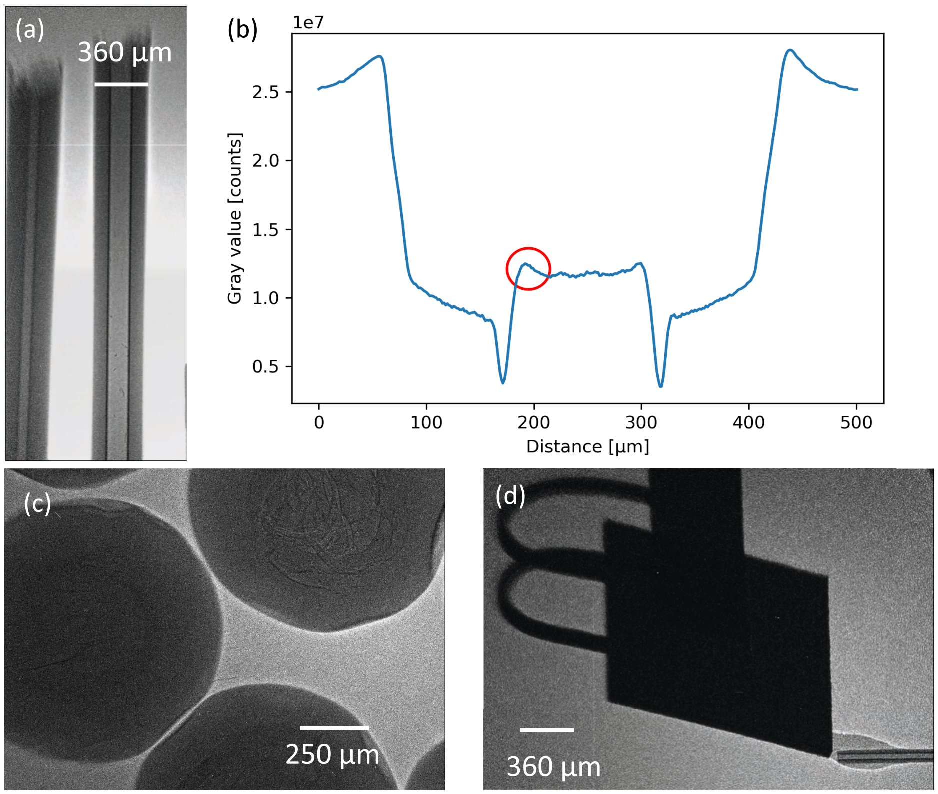

Fig. 10. High resolution radiographs showing phase contrast imaging. (a) Radiograph of two capillary tubes with inner diameters of 74.4 µm and 149.6 µm taken with the full beam. (b) A vertically summed lineout of the 149.6 µm inner diameter capillary tube is shown to the right. Clear edge enhancement can be seen at the interface. (c) Radiograph of 1 mm diameter sodium polyacrylate spheres with the half beam. (d) Radiograph of capacitive target taken with the annular beam.

7. Conclusions

Our results demonstrate that betatron X-rays generated at the ZEUS laser facility are well suited for high-resolution, single-shot radiography of dense targets, allowing for multiple angles and temporal delays. Using apodized laser near fields, including half-beam and annular profiles, we produced high-energy betatron sources with sufficient brightness to image through millimeter-scale aluminum and tungsten shielding. Radiographs of macroscopic objects, including cameras and vacuum gauges, confirm photon energies exceeding 100 keV. Additionally, µm-scale resolution was achieved using an X-ray CCD, enabling phase contrast imaging of capillary structures and

Optics EXPRESS

internal defects in NIF-scale surrogate targets. These results establish apodized betatron sources as a versatile tool for high-resolution, high-energy-density plasma diagnostics.

Funding. National Science Foundation (1935950, 2126181); U.S. Department of Energy (DE-NA0004146, PHY-2308982, DMR-1548924, PHY-2329970); U.S. Department of Energy (DE-SC0023504).

Acknowledgment. We would like to acknowledge S. Klein of Michigan Target Research and Fabrication (MiTRF) for lending us the capacitive target to image and H. LeFevre for fruitful discussions of applications and paths towards possible realization of those applications.

Disclosures. The authors declare no conflicts of interest.

Data availability. Data underlying the results presented in this paper are not publicly available at this time but may be obtained from the authors upon reasonable request.

References

1. T. Tajima and J. M. Dawson, "Laser electron accelerator," Phys. Rev. Lett. **43**(4), 267–270 (1979).
2. C. Danson, D. Hillier, N. Hopps, *et al.*, "Petawatt class lasers worldwide," High Power Laser Sci. Eng. **3**, e3 (2015).
3. E. Esarey, C. B. Schroeder, and W. P. Leemans, "Physics of laser-driven plasma-based electron accelerators," Rev. Mod. Phys. **81**(3), 1229–1285 (2009).
4. A. Gonsalves, K. Nakamura, J. Daniels, *et al.*, "Petawatt laser guiding and electron beam acceleration to 8 gev in a laser-heated capillary discharge waveguide," Phys. Rev. Lett. **122**(8), 084801 (2019).
5. C. Aniculaesei, T. Ha, S. Yoffe, *et al.*, "The acceleration of a high-charge electron bunch to 10 gev in a 10-cm nanoparticle-assisted wakefield accelerator," Matter Radiat. Extremes **9**(1), 014001 (2024).
6. J. Götzfried, A. Döpp, M. Gilljohann, *et al.*, "Physics of high-charge electron beams in laser-plasma wakefields," Phys. Rev. X **10**(4), 041015 (2020).
7. D. Guénot, D. Gustas, A. Vernier, *et al.*, "Relativistic electron beams driven by khz single-cycle light pulses," Nat. Photonics **11**(5), 293–296 (2017).
8. F. Salehi, A. Goers, G. Hine, *et al.*, "Mev electron acceleration at 1 khz with $<$ 10 mj laser pulses," Opt. Lett. **42**(2), 215–218 (2017).
9. S. P. Mangles, C. Murphy, Z. Najmudin, *et al.*, "Monoenergetic beams of relativistic electrons from intense laser–plasma interactions," Nature **431**(7008), 535–538 (2004).
10. J. Faure, Y. Glinec, A. Pukhov, *et al.*, "A laser–plasma accelerator producing monoenergetic electron beams," Nature **431**(7008), 541–544 (2004).
11. C. Geddes, C. Toth, J. Van Tilborg, *et al.*, "High-quality electron beams from a laser wakefield accelerator using plasma-channel guiding," Nature **431**(7008), 538–541 (2004).
12. S. Corde, K. Ta Phuoc, G. Lambert, *et al.*, "Femtosecond x rays from laser-plasma accelerators," Rev. Mod. Phys. **85**(1), 1–48 (2013).
13. F. Albert and A. G. Thomas, "Applications of laser wakefield accelerator-based light sources," Plasma Phys. Controlled Fusion **58**(10), 103001 (2016).
14. S. Fourmaux, S. Corde, K. T. Phuoc, *et al.*, "Single shot phase contrast imaging using laser-produced betatron x-ray beams," Opt. Lett. **36**(13), 2426–2428 (2011).
15. S. Kneip, C. McGuffey, J. L. Martins, *et al.*, "Bright spatially coherent synchrotron x-rays from a table-top source," Nat. Phys. **6**(12), 980–983 (2010).
16. A. E. Hussein, N. Senabulya, Y. Ma, *et al.*, "Laser-wakefield accelerators for high-resolution x-ray imaging of complex microstructures," Sci. Rep. **9**(1), 3249 (2019).
17. C. I. Hojbota, M. Mirzaie, D. Y. Kim, *et al.*, "High-energy betatron source driven by a 4-pw laser with applications to non-destructive imaging," Eur. Phys. J. A **59**(10), 247 (2023).
18. R. Hollinger, S. Wang, S. Zahedpour Anaraki, *et al.*, "Laser-driven high-resolution mev x-ray tomography," Optica **12**(3), 433–436 (2025).
19. Y. Glinec, J. Faure, L. L. Dain, *et al.*, "High-resolution γ-ray radiography produced by a laser-plasma driven electron source," Phys. Rev. Lett. **94**(2), 025003 (2005).
20. E. Esarey, B. Shadwick, P. Catravas, *et al.*, "Synchrotron radiation from electron beams in plasma-focusing channels," Phys. Rev. E **65**(5), 056505 (2002).
21. J. C. Wood, D. Chapman, K. Poder, *et al.*, "Ultrafast imaging of laser driven shock waves using betatron x-rays from a laser wakefield accelerator," Sci. Rep. **8**(1), 11010 (2018).
22. A. M. Angulo, S. R. Nagel, C. M. Huntington, *et al.*, "Design of a high-resolution rayleigh-taylor experiment with the crystal backlighter imager on the national ignition facility," J. Instrum. **17**(02), P02025 (2022).
23. A. Do, A. Angulo, S. Nagel, *et al.*, "High spatial resolution and contrast radiography of hydrodynamic instabilities at the national ignition facility," Phys. Plasmas **29**(8), 080703 (2022).
24. A. Do, A. Angulo, G. Hall, *et al.*, "X-ray imaging of rayleigh–taylor instabilities using fresnel zone plate at the national ignition facility," Rev. Sci. Instrum. **92**(5), 053511 (2021).
25. F. Doss, E. Loomis, L. Welser-Sherrill, *et al.*, "Instability, mixing, and transition to turbulence in a laser-driven counterflowing shear experiment," Phys. Plasmas **20**(1), 012707 (2013).

Optics EXPRESS

26. A. Ravasio, M. Koenig, S. Le Pape, *et al.*, "Hard x-ray radiography for density measurement in shock compressed matter," Phys. Plasmas **15**(6), 060701 (2008).
27. E. Dewald, K. Campbell, R. Turner, *et al.*, "Dante soft x-ray power diagnostic for national ignition facility," Rev. Sci. Instrum. **75**(10), 3759–3761 (2004).
28. L. Jarrott, L. Benedetti, H. Chen, *et al.*, "Hotspot electron temperature from x-ray continuum measurements on the nif," Rev. Sci. Instrum. **87**(11), 11E534 (2016).
29. M. Mirzaie, C. I. Hojbota, D. Y. Kim, *et al.*, "All-optical nonlinear compton scattering performed with a multi-petawatt laser," Nat. Photonics **18**(11), 1212–1217 (2024).
30. S. Steinke, J. Van Tilborg, C. Benedetti, *et al.*, "Multistage coupling of independent laser-plasma accelerators," Nature **530**(7589), 190–193 (2016).
31. J. Luo, M. Chen, W. Wu, *et al.*, "Multistage coupling of laser-wakefield accelerators with curved plasma channels," Phys. Rev. Lett. **120**(15), 154801 (2018).
32. D. Ursescu, O. Tesileanu, D. Balabanski, *et al.*, "Extreme light infrastructure nuclear physics (eli-np): present status and perspectives," in *High-Power, High-Energy, and High-Intensity Laser Technology; and Research Using Extreme Light: Entering New Frontiers with Petawatt-Class Lasers*, vol. 8780 (SPIE, 2013), pp.212–218.
33. J. Bromage, S.-W. Bahk, M. Barczys, *et al.*, "Laser system design and critical technologies for the nsf opal project," in *High-power, High-energy Lasers, and Ultrafast Optical Technologies II*, vol. 13532 (SPIE, 2025), pp.20–22.
34. T. Laurence, D. Alessi, E. Feigenbaum, *et al.*, "Mirrors for petawatt lasers: Design principles, limitations, and solutions," J. Appl. Phys. **128**(7), 071101 (2020).
35. M. O. Sanchez, "A summary of hybrid-cmos (hcmos) imaging sensor development at sandia national laboratories," Tech. rep., Sandia National Lab.(SNL-NM), Albuquerque, NM (United States) (2019).
36. R. D'Arcy, J. Chappell, J. Beinortaite, *et al.*, "Recovery time of a plasma-wakefield accelerator," Nature **603**(7899), 58–62 (2022).
37. C. McGuffey, A. Thomas, W. Schumaker, *et al.*, "Ionization induced trapping in a laser wakefield accelerator," Phys. Rev. Lett. **104**(2), 025004 (2010).
38. B. S. White, M. E. Shafer, W. H. Russel, *et al.*, "Digital detector array image quality for various gos scintillators," in *European Conference of Non-Destructive Testing*, (2018).
39. O. J. Finlay, J. Gruse, C. Thornton, *et al.*, "Characterisation of a laser plasma betatron source for high resolution x-ray imaging," Plasma Phys. Controlled Fusion **63**(8), 084010 (2021).
40. M. Berger, "Xcom: photon cross sections database," http://www.nist.gov/pml/data/xcom/index.cfm (2010).
41. S. Corde, C. Thaury, K. T. Phuoc, *et al.*, "Mapping the x-ray emission region in a laser-plasma accelerator," Phys. Rev. Lett. **107**(21), 215004 (2011).
42. N. Lopes, J. Cole, K. Poder, *et al.*, "Measurement of the lwfa betatron source length by cross-correlations over images of granular random targets, Science and Technology Facilities Council-Central Laser Facility, Annual Report," (2016).
43. B. Guo, X. Zhang, J. Zhang, *et al.*, "High-resolution phase-contrast imaging of biological specimens using a stable betatron x-ray source in the multiple-exposure mode," Sci. Rep. **9**(1), 7796 (2019).
44. M. Vargas, W. Schumaker, Z. He, *et al.*, "X-ray phase contrast imaging of additive manufactured structures using a laser wakefield accelerator," Plasma Phys. Controlled Fusion **61**(5), 054009 (2019).